Journal of Materials Processing Tech. 294 (2021) 117133

Contents lists available at ScienceDirect

Journal of Materials Processing Tech.

journal homepage: www.elsevier.com/locate/jmatprotec

On the effect of pilot holes on the mechanical behaviour of flow-drill screw joints. Experimental tests and mesoscale numerical simulations

Miguel Costas [a,*], David Morin [a], Johan Kolstø Sønstabø [b], Magnus Langseth [a]

[a] Structural Impact Laboratory (SIMLab) and Centre for Advanced Structural Analysis (CASA), Department of Structural Engineering, Norwegian University of Science and Technology (NTNU), NO-7491 Trondheim, Norway
[b] Multiconsult AS, Nedre Skøyen vei 2, 0276 Oslo, Norway

ARTICLE INFO

Associate Editor: Erhan Budak

Keywords:
Flow-drill screws
Pilot holes
Experimental testing
Finite element modelling

ABSTRACT

This research work investigated in detail the mechanical performance of a flow-drill screw connection of two aluminium plates with and without pilot holes. An extensive experimental campaign involving material and joint tests under different loading modes is presented. These tests are supported by numerical models. Detailed solid-element models provided meaningful information about the local deformation mechanisms of the tested configurations, and allowed to identify the reason behind the early screw failure observed in some of the experimental joint tests. Moreover, several geometrical features of the connection were found to be relevant for the mesoscopic model, so their influence was assessed. The combination of experiments and simulations provided robust and meaningful understanding of the connections.

1. Introduction

Structural analysis strongly relies on adequate material models and trustworthy representations of the connections between different structural members. Whilst a considerable effort is usually put into the former, correct characterisation and modelling of structural joints is in general disregarded. The reason for this is that joints are traditionally oversized in structural design in order to transfer the deformation to the joining members.

However, there are cases where oversizing is not an option and joint failure must be considered, for instance in car crash analysis. Ligh-weighting has gained huge momentum in the automotive industry, leading to the integration of thinner, lighter and mixed materials. The increasing use of these materials has created new challenges when it comes to joining, and a large number of different joining techniques can be found in a vehicle produced nowadays.

Among these techniques, joining with flow-drill screw (FDS) connections is becoming more and more popular. In contrast to other joining methods like spot welding, flow-drill screws enable connections of dissimilar materials. Moreover, while most fastening options require two-sided access, flow-drill screws are installed from one side only. This makes the technology particularly attractive for assembly into hydroformed or extruded profiles, or into locations with difficult access. Fig. 1 illustrates different stages of the joining process of two metal sheets, which usually takes between 1.5 and 4 s depending on thicknesses, materials and screw type. The screw spinning at elevated speed heats up and perforates the plates as it is pushed down, creating a thread in the partially melted material that flows up and downwards along the length of the screw. The process ends when the head hits the top plate and a final torque is applied to tighten the connection. A hole is customarily machined in the top plate prior to the installation of the flow-drill screw, usually called *pre-hole*, *pilot hole* or *clearance hole*. This gap hosts the material flowing upwards during the penetration of the screw, increasing the usable threaded length. Flow-drill screw joints without pilot hole are also feasible, provided that the screw head is hollow to host the boss. There are no existing studies on the effects of said holes on the mechanical performance of flow-drill screw connections and they are the focus of the present work.

In spite of becoming a popular joining technique, the number of experimental works focused on the mechanical behaviour of flow-drill screws is still quite limited. Szlosarek et al. (2013) carried out a testing campaign characterising flow-drill screw connections of carbon fibre and aluminium plates under tension and shearing, where the connections incorporated a pilot hole in the top carbon fibre plate. They

* Corresponding author.
E-mail addresses: miguel.costas@ntnu.no (M. Costas), david.morin@ntnu.no (D. Morin), joks@multiconsult.no (J.K. Sønstabø), magnus.langseth@ntnu.no (M. Langseth).

https://doi.org/10.1016/j.jmatprotec.2021.117133
Received 17 September 2020; Received in revised form 22 February 2021; Accepted 28 February 2021
Available online 4 March 2021

presented a novel testing rig where the loading angle could be changed, and displacements were optically measured to omit the flexibility of the rig. Skovron et al. (2014) investigated the influence of the process parameters on the geometry of flow-drill screw joints with pilot holes, outlining the feasibility of the different results by mechanical testing. Sønstabø et al. (2015) presented experimental joint and component tests of flow-drill screws with pilot holes connecting two AA6016-T4 aluminium plates, and compared their performance to that of self-piercing rivets. Skovron et al. (2015) investigated the effect of pre-heating the plates with an external source before installing the screws, assessing it with mechanical tests of joints in AA6063-T5A aluminium plates without pilot holes. They showed that preheating the material reduced the process time and the torque, but they also suggested that the temperature should be limited to prevent harmful effects on the mechanical behaviour. Aslan et al. (2019) recently presented additional information on the effect of the process in the joint geometry. They investigated a mixed connection of an AA5182-O aluminium alloy and a DP600 steel with pilot holes in the top plate, showing that it is possible to modify the process conditions in order to improve the material ductility and prevent crack defects.

As it will be discussed in this work, experimental testing of joints is complex and not free of difficulties. Finite element simulations can potentially reduce the number of tests required to characterise a certain joint. However, these finite element models must reproduce in great detail the geometry and the material properties of the joint in order to be reliable. The herein called *mesoscopic models* are finite element models built with a very refined mesh of solid elements that accurately reproduces the geometrical features of the connection. The prefix *meso-* is used to indicate that the models do not account for microstructural or micromechanical features such as grains, but are very refined compared to finite element models used in industrial applications. A literature review reveals a number of research works focused on the mesoscopic modelling of different types of structural joints. Bouchard et al. (2008) developed mesoscopic models for self-piercing riveting connections, including the simulation of the riveting process. Their results are useful from an industrial point of view because they enable to predict the feasibility of a certain configuration depending on the number and thickness of sheets, material, rivet geometry and lower tool. Chen et al. (2014) also built mesoscopic models for rivets, but focusing on the prediction of failure and the development of predictive formulas. The notable differences between their predictions and tests confirm the complexity of this modelling strategy. Compared to that of flow-drilling screws, the assembly process of self-piercing rivets is purely mechanical and does not imply thermal softening, which makes its simulation more manageable. Nevertheless, Liu et al. (2020) have recently attempted a mesoscopic simulation of the forming process of a FDS steel-aluminium connection with pilot hole. Mesoscopic models for spot welds can also be found in the literature: Kong et al. (2008) built a detailed finite element model of the single lap test of a spot weld with different material models around the connection. The model was used further to study the influence of the nugget size and the sheet thickness. Nielsen (2008) provided deeper understanding of the material properties around the weld using a porous plasticity model to simulate plug failure. His models predicted the mechanical response of the connections quite well, but did not properly capture damage propagation. In order to improve this point, Nielsen and Tvergaard (2010) incorporated a modification in Gurson's porous plasticity model. Pandya et al. (2020) recently built mesoscopic models to support a testing campaign on the ultimate load-bearing capacity of spot welds in dual-phase steels. Although Kim et al. (2020) recently proposed alternative modelling technologies such as artificial neural networks to study flow-drill screw connections, mesoscopic modelling of the mechanical behaviour of said joints has not been studied in detail so far. To the best of the authors' knowledge, Sønstabø et al. (2018a) published the only work dealing with this topic up to date, where the they develop a mesoscopic model of a flow-drill screw connection with pilot hole and use it to characterise the mechanics of the joint.

The present investigation combines experimental testing and advanced finite element modelling techniques to study flow-drill screw connections. In particular, the work contributes by assessing the influence of pilot holes on the mechanical response of the joints under different loading configurations. Moreover, the influence of several geometrical parameters of the connection on the predictions of mesoscopic models are reported and discussed.

2. Description of the studied joints

The research presented in this paper places a focus on the mechanical behaviour of structural joints consisting of two aluminium plates joined together with a flow-drill screw made of case-hardened, high-strength steel. The top plate that is in contact with the head of the screw is made of an AA6060-T6 aluminium alloy with a nominal thickness of 2.5 mm, whereas the bottom plate is made of AA6063-T4 with a nominal thickness of 2.0 mm. The screw model was M5×20/751-9132-609, by Ejot.

Two different configurations of this joint were studied, one with a pilot hole of diameter 8 mm that was machined in the top plate before the screw was inserted, and another with the screw directly applied without any preparation of the aluminium plates. Fig. 2 illustrates both configurations.

The plates used for the specimens were cut from extruded profiles using wire electrical discharge machining (EDM) inside a pool of deionised water to minimise alterations in the material. The screws were M5 × 20, case-hardened steel flow-drill screws with a total length of 24 mm, including a head of 4 mm. The maximum diameter of the head (closest to the plates) was 13 mm, see Fig. 2. The samples were fastened by Ejot in Germany.

Samples of joints with and without pilot hole were cut in half using EDM to reveal the geometry of the connections, which is shown in Fig. 3a and b. It can be seen how the screws made the aluminium flow up and downwards as it perforated the plates. The material flowing downwards is usually called *extrusion* or *bushing*, while the material being pushed upwards is called *boss* or *burr*. In this study the terms *extrusion* and *boss* are employed. The cutaway view in Fig. 3b also shows how the hollow head of the screw makes way for the upwards flow, and how the bottom plate bends due to the flow of aluminium between both plates. This curvature can occur in flow-drill screw connections without

Fig. 1. Illustration of the flow-drill process with a pilot hole in the top plate. Adapted from Sønstabø et al. (2015).

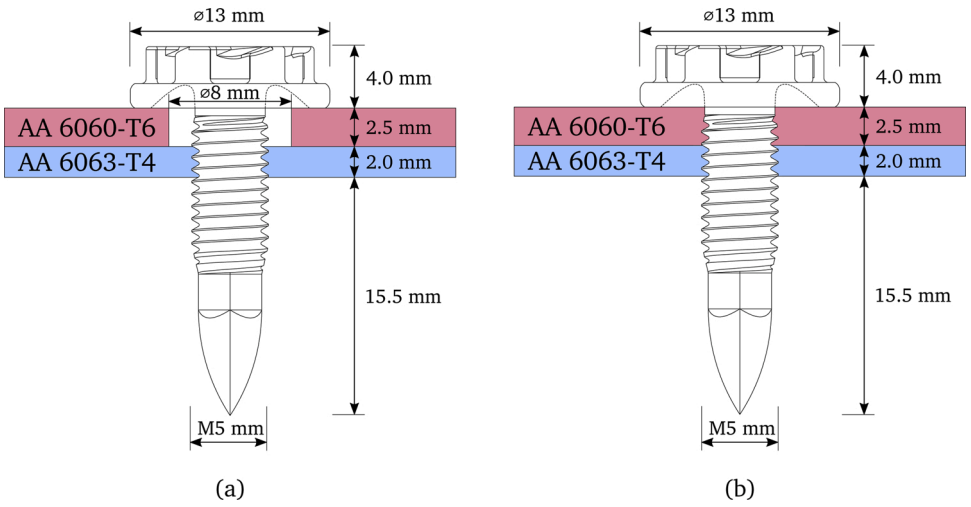

Fig. 2. Schematic representation of the studied joint configurations with (a) and without (b) pilot hole in the top plate. The extrusion formed during the process has been omitted for simplification. Dimensions in millimetres.

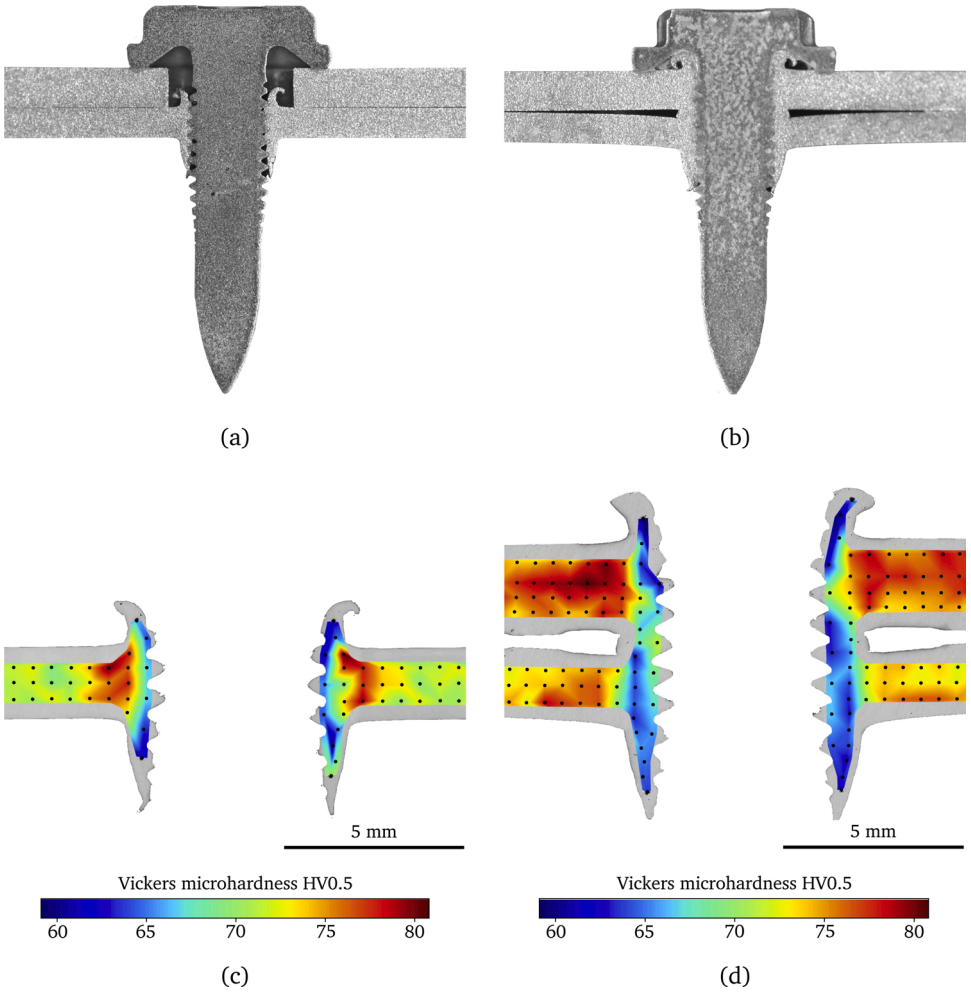

Fig. 3. Cutaway view of samples with (a) and without (b) pilot hole, and microhardness contour plots in the vicinity of the thread in the pilot hole (c) and non pilot hole (d) configurations, where the top plate with the pilot hole has been omitted. The location of the Vickers indentations is marked with black dots and the colour maps correspond to interpolated values. (For interpretation of the references to color in this figure legend, the reader is referred to the web version of this article.)

pilot holes, generally affecting the plate with a lower stiffness. Lastly and significantly the pictures show that the screw was not totally engaged to the thread in the bushings, especially in the configuration with a pilot hole. This point will be elaborated in the section dedicated to the mesoscopic model of the connection.

An elevated number of HV0.5 Vickers microhardness tests with a

load of 500 gf (around 300 tests in total) were performed on the cut samples in order to map the hardness of the aluminium plates in the vicinity of the connection. This is relevant for the mesoscopic models of the connection, that may include detailed material properties. The microhardness results are plotted as colour maps in Fig. 3c and d superimposed to the cutaway view, where dots indicate the measuring points. The screw was removed from the pictures together with the top plate with a hole, since the latter was not affected by the flow-drilling process.

The pictures show how the aluminium closest to the screw was clearly altered during the formation of the thread, but also hardened at approximately 1 mm away from the interface with the screw. This hardening was particularly noticeable in the bottom plate, and can be explained by two reasons. Firstly, the 6063 alloy in the bottom plate is in T4 condition (naturally aged), and the 6060 alloy in the top plate is in condition T6 (aged to peak strength). Temper T4 provides more potential for precipitation than T6, as shown by Engler et al. (2019), and therefore the temperatures reached during the penetration of the screw could have contributed to generate precipitates in the bottom plate that affected the yield stress and work-hardening of the alloy. Skovron et al. (2014) reported temperatures between 150 and 330 °C during the flow drilling process, with a duration between 1.5 and 4 s. Under these conditions early stage precipitation occurs, whereby only Guinier-Preston (GP) zones and clusters are expected to increase, see Khadyko et al. (2019). However, this would be enough to give some additional strength to the alloy. Secondly, the 6063-T4 alloy underwent more work-hardening during plastic deformation than 6060-T6, as it will be shown on next chapter. This means that plastic deformations caused during the penetration of the screw could have hardened the material, especially in the bottom plate.

Sønstabø et al. (2018a) performed hardness tests on a similar FDS connection with pilot hole, but using a 6063 alloy in temper T6 for the bottom plate. Comparison between their tests and those provided in Fig. 3c reveals that the hardness of the 6063-T4 plates used in the current investigation was much more affected by the assembly process than those reported by Sønstabø et al. (2018a), in temper T6. This supports the hypotheses stated in the previous paragraph.

3. Material tests and constitutive modelling

3.1. Aluminium plates

Tensile tests were carried out for both alloys used in this investigation, namely AA6060-T6 and AA6063-T4. Flat tensile specimens with the dimensions shown in Fig. 4a were extracted from the profiles parallel to the extrusion direction using wire-cut electrical discharge machining (EDM) to reduce the overheating of the materials. The thicknesses of the specimens were 2.5 mm for the 6060-T6 and 2.0 mm for the 6063-T4; the same as the plates they were respectively extracted from. The specimens had different sizes because they were machined for two previous, originally independent, testing campaigns. The gauges of the specimens were painted with a black-and-white speckle pattern so that a digital image correlation (DIC) software could be used to measure the surface strains. The in-house DIC software eCorr was used, which is described in Fagerholt et al. (2013). Three repetitions were run for each alloy in an Instron 5982 at 0.67 and 1.0 mm/min for the AA6060-T6 and AA6063-T4 alloys, respectively, to maintain the same initial strain rate. The tests were recorded at two frames per second with a Prosilica GC2450 camera with an approximate resolution of 120 pixels per millimetre. Virtual extensometers with lengths of 9.87 mm for the AA6060-T6 alloy and 16.74 mm for the AA6063-T4 alloy were used in the DIC software to compute the engineering strains. The obtained engineering stress–strain curves are provided in Fig. 4b, where a good repeatability was observed in both materials.

Both alloys were modelled with the same constitutive relation consisting of an isotropic, hypoelastic-plastic material model implemented in Abaqus/Explicit 2019 with user-defined subroutines, Simulia (2018). Although Sønstabø et al. (2016, 2018b) reported moderate anisotropy of both aluminium alloys, an isotropic model was chosen due to its simplicity.

Assuming additive decomposition of strains, the strain rate tensor $\mathbf{D}$ can be written as

$$\mathrm{D} = \mathrm{D}^{\mathrm{e}} + \mathrm{D}^{\mathrm{p}}, \tag{1}$$

where the superindices “e” and “p” indicate the elastic and plastic contributions, respectively. Provided that elastic deformations are relatively small, the elastic part of the strain rate tensor can be written in terms of the Green-Naghdi stress rate as

$$\mathbf{D}^{\mathrm{e}} = \frac{1+\nu}{E}\boldsymbol{\sigma}^{\nabla \mathrm{G}} - \frac{\nu}{E}\mathrm{tr}\left(\boldsymbol{\sigma}^{\nabla \mathrm{G}}\right)\mathbf{I}, \tag{2}$$

where E is the elastic modulus, ν is the Poisson’s ratio, $\boldsymbol{\sigma}^{\nabla \mathrm{G}}$ is the Green-Naghdi stress rate of the Cauchy stress tensor $\boldsymbol{\sigma}$, and $\mathbf{I}$ is the identity tensor. An elastic modulus of 70 GPa and a Poisson’s ratio of 0.33 were assumed.

The plastic strain rate tensor $\mathbf{D}^{\mathrm{p}}$ is computed from the flow rule. Adopting associated plastic flow, the yield function f serves as a flow

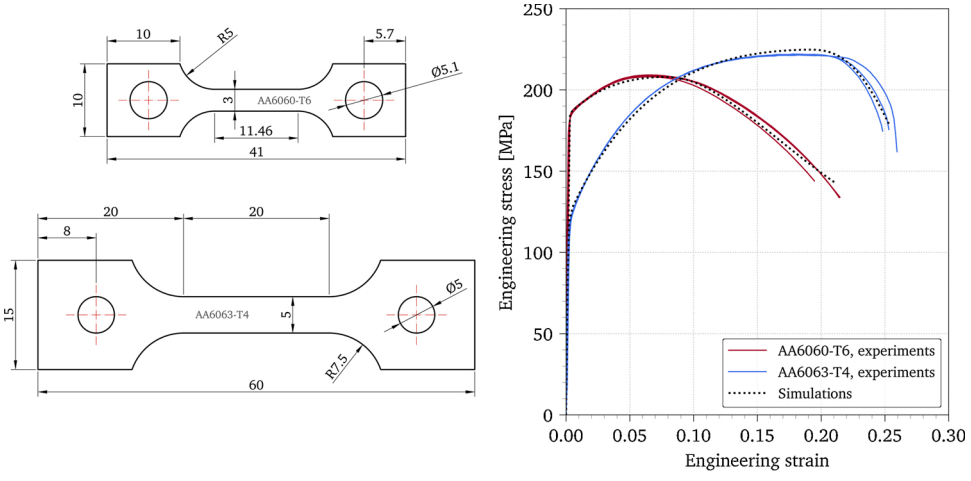

(a) (b)

Fig. 4. Dimensions of the tensile specimens extracted from the profiles (a) and engineering stress–strain curves of the aluminium alloys (b).

potential. Thus, $\mathbf{D}^{\mathrm{p}}$ is expressed as

$$\mathbf{D}^{\mathrm{p}} = \dot{\lambda}\frac{\partial f}{\partial \boldsymbol{\sigma}}, \tag{3}$$

where $\dot{\lambda}$ is the plastic multiplier and f is the yield function, which can be written as

$$f = \sigma_{\mathrm{eq}} - (\sigma_0 + R) \leq 0, \tag{4}$$

where σ_{eq} is the equivalent stress, σ_0 is the initial yield stress, and R represents the isotropic hardening. The Hosford-Hershey yield surface was adopted for both alloys with an exponent of $m = 8$. Barlat et al. (2005) showed that this exponent is adequate for face-centred cubic crystalline structure alloys (FCC). Adopting this yield surface instead of von Mises' was considered a good compromise between accuracy and calibration effort. It is also worth mentioning that additional simulations run with Mises' surface showed no noticeable difference in the results for this particular case. With Hosford-Hershey's criterion, the equivalent stress in Eq. (4) can be defined in terms of the ordered principal stresses σ_1, σ_2, and σ_3 as

$$\sigma_{\mathrm{eq}} = \left[\frac{1}{2}\left(|\sigma_1 - \sigma_2|^m + |\sigma_2 - \sigma_3|^m + |\sigma_3 - \sigma_1|^m\right)\right]^{\frac{1}{m}}. \tag{5}$$

Work-hardening R was represented by an extended Voce law with three pairs of terms, reading

$$R = \sum_{i=1}^{3} Q_i\left[1 - \exp\left(-\frac{\theta_i}{Q_i}p\right)\right], \tag{6}$$

where Q_i represent the saturation stresses, θ_i are the initial hardening moduli, and p is the equivalent plastic strain. The parameters Q_i and θ_i were calibrated using inverse modelling of the tensile tests in Abaqus/Standard 2019, where the tensile specimens were modelled with 10 solid elements through the thickness and taking advantage of the three symmetry planes. The identification was done in LS-OPT, see Livermore (2015), providing the parameters shown in Table 1. The experimental engineering stress-strain curves are compared with the calibrated numerical simulations in Fig. 4b.

Damage was accounted for using the uncoupled damage evolution rule proposed by Cockcroft and Latham (1968), where the damage variable D is computed as

$$D = \int \frac{1}{W_{\mathrm{c}}}\left\langle \sigma_1 \right\rangle \mathrm{d}p, \tag{7}$$

where W_{c} is an experimentally determined parameter, σ_1 is the major principal stress, and $\langle \bullet \rangle$ represents the Macaulay brackets defined as $\langle x \rangle = \max(0, x)$. Note that this formulation implies that damage is only accumulated when the first principal stress is positive. This criterion has the advantage of being simple to calibrate, since the parameter W_{c} is readily obtained from the inverse model of the tensile tests integrating the first principal stress over the equivalent plastic strain up to failure in the centremost element of the neck. While being simple, the Cockcroft-Latham criterion was shown to give reasonable predictions of damage in the mesoscopic models of flow-drill screws developed by Sønstabø et al. (2018a), where the element size was in the same order of magnitude as that in the present investigation. The values of the Cockcroft-Latham parameters obtained from the inverse models are given in Table 1.

While the hardness maps shown in Fig. 3 indicate variable material properties in the aluminium plates near the screw, constant material properties were adopted for each aluminium alloy. The reason for this was that a direct link between hardness and initial yield stress, work-hardening and failure cannot be safely established due to the elevated plastic strains developed in the aluminium plates during the installation of the screws. Myhr et al. (2015) showed that the interaction of heat treatment and residual plastic strains leads to very complex dislocation and precipitation mechanisms, thus deeming the current assumption reasonable. Sønstabø et al. (2018a) successfully applied this simplification to a similar connection investigated in a previous work.

3.2. High-strength steel screw

The screws used in this investigation were made of case-hardened steel. Case-hardening had the effect of creating an outer layer with different properties compared to the inner core. In order to account for this difference, two separate models were calibrated. The small size of the screws presented an additional challenge for the correct calibration of both mechanical behaviours. The strategy followed in this investigation consisted of testing and calibrating the steel in the core of the screw, and then estimating the yield stress of the outer hardened layer using the ratio of the Vickers hardness of the inner and outer materials.

Screw failure was observed in some of the joint tests run for this investigation, so it was necessary to include and calibrate a failure criterion in order to reproduce the behaviour in the numerical simulations. This criterion had to be calibrated for the inner and outer materials, using tensile tests for the former and bending tests for the latter.

Firstly, microscopy images of a section of the screw conveniently polished and etched were analysed to determine the deepness of the hardened layer. The sample was embedded in Bakelite, roughed down with silicon carbide sanding belts of P320, polished with lubricated cloths and diamond paste of 9, 3 and 1 micrometers, and finally etched with Nital 2% (98 ml ethanol + 2 ml HNO_3) during 15–30 s. It was observed that the deepness of the hardened layer was not homogeneous, with values between 250 and 700 μm (see Fig. 5a and 5 b), even though the boundary between case-hardened and base material is quite diffuse. Then, cylindrical tensile specimens with threaded grips were designed and machined from the inside of the screws in a way such that their gauges were completely outside the case-hardened area. The dimensions of the specimens are provided in Fig. 5c together with an illustration of the location of the specimens inside the screw.

The tensile specimens were tested at 0.5 mm/min in an Instron 5982. Strains were measured using DIC by tracking a pair of dots painted on the surface of the specimens with an initial separation of 7 mm. Additional measurements of the strains were done by edge tracing and using a physical extensometer, but none of them gave as good results as tracking the markers on the specimens. The engineering stress-strain curves are presented in Fig. 5d.

The constitutive relation adopted for the steel in the screw was the same as that used for the aluminium alloys however with Hershey's yield surface changed to von Mises'. The elastic modulus was set to 210 GPa and the Poisson's ratio was set to 0.3. Inverse models of the tensile tests were used to calibrate the initial yield stress, the work-hardening, and the Cockcroft-Latham failure parameter of the steel

Table 1
Parameters of the extended Voce hardening rule and the Cockcroft-Latham damage criterion for both aluminium alloys, the steel inside the screw and the hardened steel, given in MPa.

Material	σ_0	Q_1	θ_1	Q_2	θ_2	Q_3	θ_3	W_{c}
AA6060-T6 (top)	183.2	2.5	5746.3	48.1	1030.3	3.5	5.5	216.0
AA6063-T4 (bottom)	111.1	11.7	13,564.6	164.6	1889.0	4.7	27.0	232.0
Steel (inside)	973.9	58.9	80,371.5	89.7	6596.3	14.6	10,437.2	480.0
Steel (hardened)	1659.8	58.9	80,371.5	89.7	6596.3	14.6	10,437.2	40.0

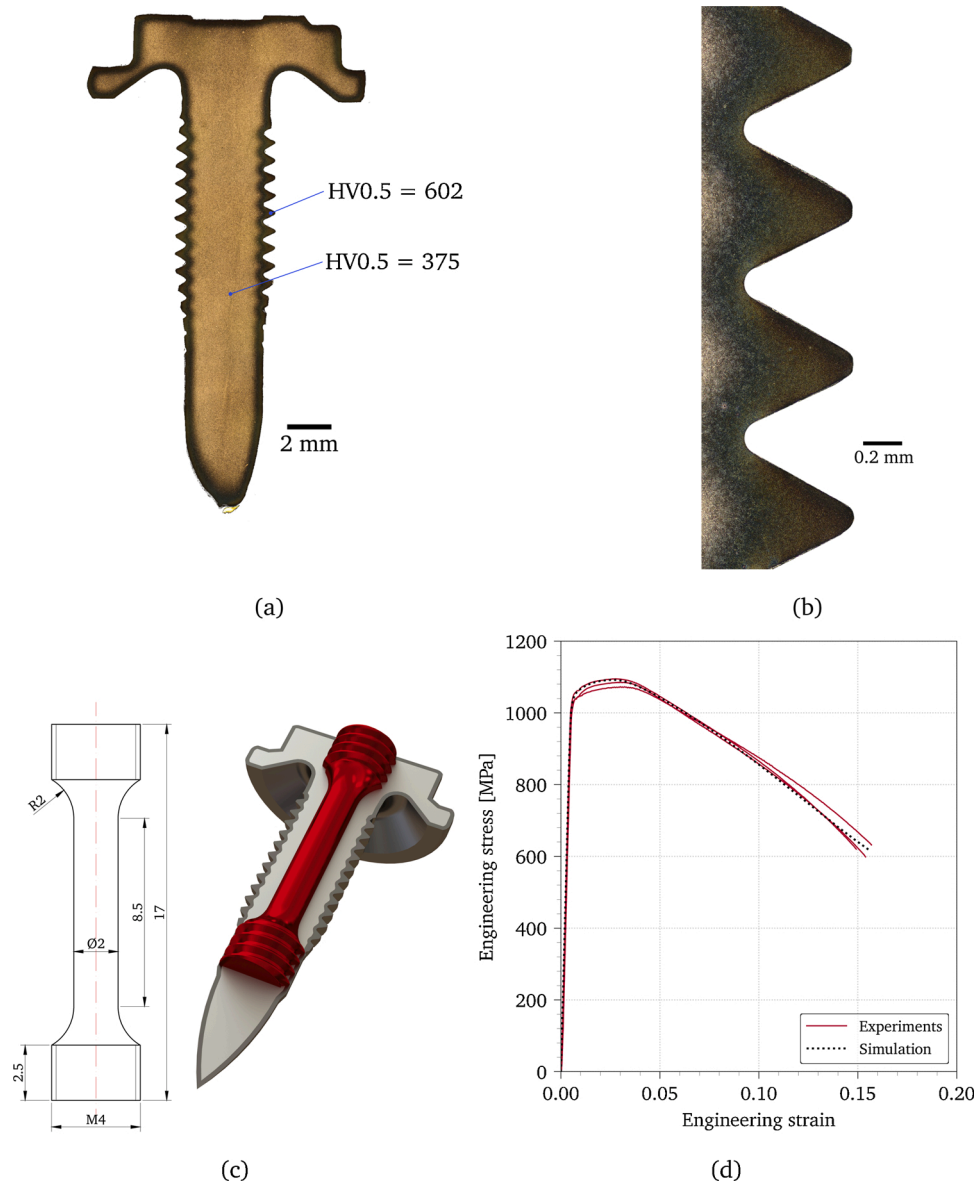

Fig. 5. Etched section of the screw revealing the case-hardened layer (a) and detail of the hardened thread (b). Dimensions in millimetres of the tensile specimens extracted from the inside of the screws (c) and engineering stress–strain curves of the material (d).

inside the screw. A detailed axisymmetric model of the tensile specimens with 20 elements over the radius of the gauge was used for determining the initial yield stress and the Voce work-hardening constants, whereas solid elements with reduced integration and an element size of 0.125 mm were used to calibrate the Cockcroft-Latham failure parameter $W_c = 480$ MPa. The same element type and size were used in the finite element models described in Section 5, as Costas et al. (2019) showed that the Cockcroft-Latham criterion is mesh-sensitive under strain localisation.

Once the mechanical properties of the inside of the screw were calibrated, the parameters corresponding to the outer hardened surface were obtained. It was first assumed that the work-hardening of the steel was the same in the hardened layer as in the core of the screw, meaning that the six Voce parameters remain the same. Holmen et al. (2017) suggested that the initial yield stress of the hardened layer could be estimated by assuming that the ratio of Vickers hardness between this layer and the inner part of the screw was equivalent to the ratio of the ultimate engineering tensile stresses of both materials, i.e.,

$$\frac{\mathrm{HV_h}}{\mathrm{HV_i}} = \frac{\mathrm{UTS_h}}{\mathrm{UTS_i}}. \tag{8}$$

Here HV means Vickers hardness, UTS stands for ultimate engineering tensile stress, and the sub-indices “h” and “i” refer to the hardened and inner parts of the screw, respectively. The UTS can be computed applying Considère’s criterion, which states that the true stress and its derivative with respect to true strain are equal at the onset of diffuse necking. If elastic strains are neglected, this criterion reads

$$\frac{\mathrm{d}\sigma_{\mathrm{eq}}}{\mathrm{d}p} = \sigma_{\mathrm{eq}}. \tag{9}$$

At yielding, the equivalent stress equals the current yield stress of the material. Using Eqs. (4) and (6),

$$\sigma_{\mathrm{eq}} = \sigma_0 + \sum_{i=1}^{3} Q_i \left[1 - \exp\left(-\frac{\theta_i}{Q_i} p\right)\right]. \tag{10}$$

Up to diffuse necking, the equivalent stress and the engineering stress s

are related through

$$\sigma_{eq} = sexp(p). \tag{11}$$

Using Eqs. (10) and (11), Eq. (9) can be re-written as

$$\sum_{i=1}^{3} \theta_i \exp\left(-\frac{\theta_i}{Q_i} p_{u,h}\right) = \frac{HV_h}{HV_i} UTS_i \exp(p_{u,h}), \tag{12}$$

where $p_{u,h}$ is the equivalent plastic strain at necking of the hardened steel. Adopting the experimental value $UTS_i = 1091.9$ MPa, Eq. (12) can be solved numerically for $p_{u,h}$. Given that the hardening parameters are considered to be the same for the inner and outer materials, it is straightforward to obtain the initial yield stress of the outer material as

$$\sigma_0 = \frac{HV_h}{HV_i} UTS_i \exp(p_{u,h}) - \sum_{i=1}^{3} Q_i \left[1 - \exp\left(-\frac{\theta_i}{Q_i} p_{u,h}\right)\right], \tag{13}$$

which gives a value of $\sigma_0 = 1659.8$ MPa for the initial yield stress of the case-hardened material.

The Cockcroft-Latham failure parameter of the hardened steel was obtained by inverse modelling of a bending test of the screw up to failure. The head of the screw was removed, and the remaining sample was cut in half and mounted into a small-scale three-point bending tool with a span of 11 mm (see Fig. 6a). The displacement was tracked by a camera and the forces were measured with a load cell. Three repetitions of the test were run. The test was then modelled in Abaqus/Explicit 2019 using a detailed model of the specimen containing the two material models calibrated previously, where the only missing parameter was the Cockcroft-Latham parameter of the hardened material. It was assumed that the hardened layer had a thickness varying between 650 μm at the thread's crests and 330 μm at its roots. These values were estimated from the etched images of the cutaway sample of the connection, see Fig. 5a and b. It is worth mentioning that the gradual transition between case-hardened and base material observed in Fig. 5c was not modelled, i.e., only two sets of material properties were used in the screw.

Considering the small displacements below 0.1 mm and the scatter in the tests, the force at failure measured with the load cell was used as target in the calibration. The three experimental samples had slightly different thicknesses, thus their forces at failure were also different, as shown in Fig. 6b. The finite element model with a thickness of exactly 2.5 mm was run with different W_c parameters in the hardened layer, providing the results plotted in Fig. 6b. A value of $W_c = 40$ MPa produced failure at the outer layer at the same point as in the experiments, so this value was adopted for the failure parameter of the hardened steel.

4. Experimental joint tests

A thorough experimental testing campaign was carried out to investigate and compare the mechanical behaviour of the FDS joints with and without pilot holes. This campaign started with cross tests at three different loading angles, namely pure tension, pure shear, and a mixed mode at 45 degrees. Sønstabø et al. (2018b) proposed the validation strategy used herein, carrying out single-lap and peeling tests as benchmark tests to corroborate the observations in the cross tests. This section provides the description of all tests and a summary of the results.

4.1. Cross tests

Cross specimens were assembled according to the dimensions shown in Fig. 7a and tested under different loading angles, namely pure shear, pure tension, and a mixed mode at 45 degrees (see Fig. 9a). All tests were performed at a constant speed of 5 mm/min.

In the cross tensile tests (pure tension), the specimens were mounted to steel parts using clamping fixtures and bolts, as shown in Fig. 8a. The assembly was then mounted into an Instron 5982 machine to run the tests. The force was measured with a load cell and the relative displacement between both steel fixtures was computed using DIC to track the position of a series of chequerboard markers glued onto the moving parts.

A custom-made test rig was used for the mixed and shear tests, consisting of a rigid steel frame hosting two sturdy steel parts inside. One of these parts was fixed to the frame while the other one was connected to the testing machine through a hinge. These steel parts are interchangeable to get shear or mixed mode loading. The frame was bolted to the platform of the testing machine to avoid any displacement during the test, and chequerboard stickers were also used in this case to track the relative displacement between the fixed and the moving part. An illustration of the rig set to 45 degrees is provided in Fig. 8b, and the working principles under mixed and shear loading modes are illustrated in Fig. 8c and d, respectively. Sønstabø et al. (2018a) described the device more comprehensively.

The resulting force-displacement curves of the cross tests are given in Fig. 9 for all configurations. Repeatability was acceptable, even though it could be observed that the specimens were not totally symmetric and the screw was misplaced ±1.5 mm with respect to the centre of the plates.

Cross-tension tests (Fig. 9b) showed only a marginal difference between specimens incorporating a pilot hole or not, with the overall ductility being somewhat higher in the latter. The failure mode for

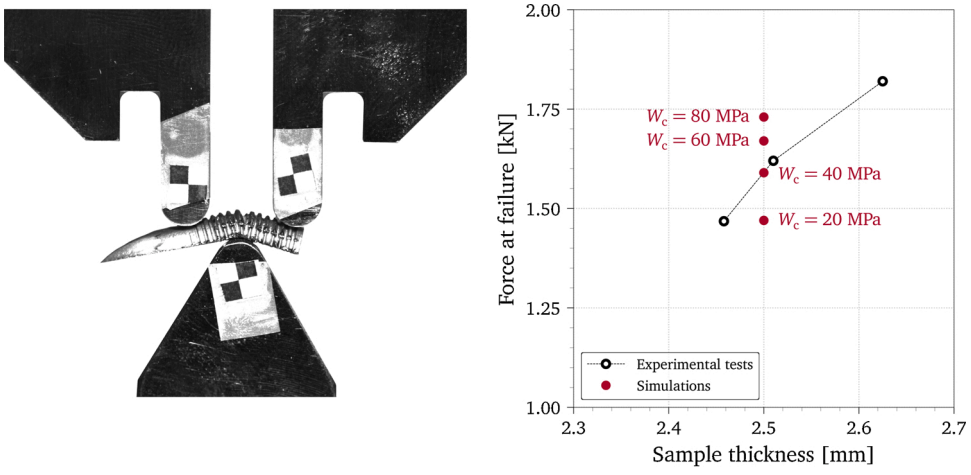

Fig. 6. Half-screw bending test (a) and calibration of the inverse model with different values of W_c in the case-hardened layer (b).

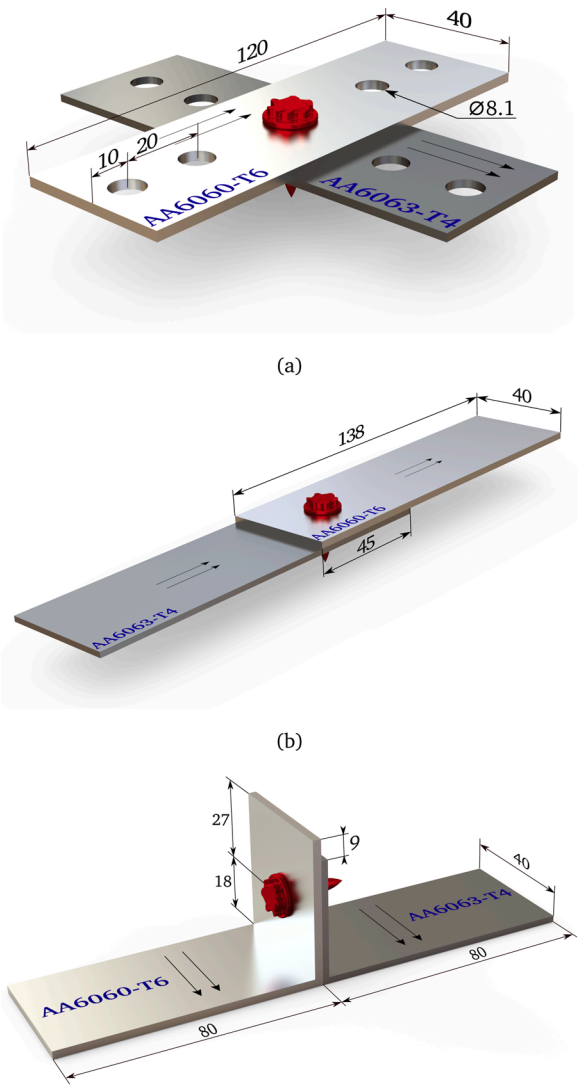

Fig. 7. Dimensions in millimetres of the joint specimens for cross tests (a), single-lap tests (b), and peeling tests (c). The two parallel arrows indicate the extrusion direction of the original aluminium profiles.

tensile loading consisted of the plates bending, especially the bottom plate which was more flexible, and the screw finally detaching from the thread of the bottom plate at the end of the tests. From the analysis of the test results, it seemed that the material extruded in the gap between the plates in the configuration without pilot hole (see Fig. 3b) was not effectively bonded and thus did not provide additional resistance to the joint. As it will be shown later on, it was the longer extrusion of the joints without pilot hole that gave the joint slightly more resistance. Detail pictures of representative post-mortem bottom plates are provided in Fig. 10a and b.

Fig. 9c shows the force-displacement curves of the cross tests loaded at 45 degrees (mixed mode). Only three successful tests were achieved with the samples without pilot hole due to additional difficulties in assembling the specimens in the rig for mixed loading. The curves show that samples incorporating a pilot hole have a lower maximum force than those without it. The failure mode consisted in a combination of the pull-out observed in the tension cross-tension cases and a through-thickness shear failure of the bottom plate. The exception to this rule is one repetition of the specimens without pilot hole where the screw snapped at the end of the test. In general, the force levels of these mixed-mode tests laid between those of pure tension and pure shear. The deformation and failure in the bottom plate are depicted in Fig. 10c and d.

This fracture was caused by the combination of bending and shear loads in the screw. In the pilot hole configuration, the presence of a pilot hole enabled the screw to rotate more freely as the plates moved away from each other. This rotational capacity caused the head of the screw to penetrate the pilot hole, and the tip of the screw to contact the bottom plate, making it bulge slightly (Fig. 10e). This prevented screw failure, as opposed to the configuration without a hole where the screw had more constraint against rotation, increasing bending and thus snapping at a certain point (Fig. 10f).

The most remarkable differences between specimens with and without pilot holes was observed in the cross-shear tests, Fig. 9d. Failure across the shank of the screw was observed in all repetitions without a pilot hole. The fracture surfaces of the screws were analysed under scanning electron microscopy (SEM) to reveal the failure mechanism. A general view of this surface is provided in Fig. 11a, where the location of detailed SEM images is indicated. The layered outer structure of the screw can be clearly observed in Fig. 11b, where the steel core, the case-hardened layer and an outer, superficial coating are depicted. Even at this magnification level it can be observed how the fracture morphology differs in the steel core and the case-hardened layer and how the superficial coating is detached from the steel. Detailed pictures of the fracture morphology at the steel core and the case-hardened layer are shown in Fig. 11c and are shown in Fig. 11d, respectively. The small, uniform dimples observed in Fig. are shown in Fig. 11c are an indicator of ductile failure under positive stress triaxialities. Notice that, even though the cross specimens were loaded under pure shear, this fracture surface indicates a tensile-dominated failure mode stemming from a combination of bending and shear loads in the screw. In the pilot hole configuration, the presence of a pilot hole enabled the screw to rotate more freely as the plates moved away from each other. This rotational capacity caused the head of the screw to penetrate the pilot hole, and the tip of the screw to contact the bottom plate, making it bulge slightly (Fig. 10e). This prevented screw failure, as opposed to the configuration without a hole where the screw had more constraint against rotation, increasing bending and thus snapping at a certain point (Fig. 10f).

On the other hand, the absence of voids in Fig. 11d indicates a much more brittle behaviour in the case-hardened layer, which is in line with the assumption of two layers of material properties made in the constitutive modelling of the screw. It will be shown later how the brittle, outer hardened layer is believed to be responsible for the screw failure in the cross-shear tests without pilot holes.

4.2. *Single-lap tests*

Single-lap tests are aimed to study the mechanical behaviour of joints under shear-dominated loading. The loading state evolves from pure shear at the beginning of the test to a combination of shear and tension as the plates deform during the test. The geometry and dimensions of the assembled single-lap specimens are shown in Fig. 7b. The tests were carried out at a speed of 10 mm/min using an Instron 8032 machine with hydraulic grips, and recorded by two Prosilica GC2450 cameras. Digital image correlation was performed using the images from one of the cameras with the aim of computing the relative displacement of the two aluminium plates. This method avoided any influence of the compliance of the machine's elements and any possible sliding at the grips.

Four repetitions were run for each of the two joint configurations, i.e., with and without pilot holes. The force-displacement curves are provided in Fig. 12a, where the initial length of the virtual extensometer attached onto the DIC pictures was 100 mm. This extensometer was centred at the screw head.

The results show the influence of the pilot hole on the mechanical behaviour of the connection. The specimens with a pilot hole showed a

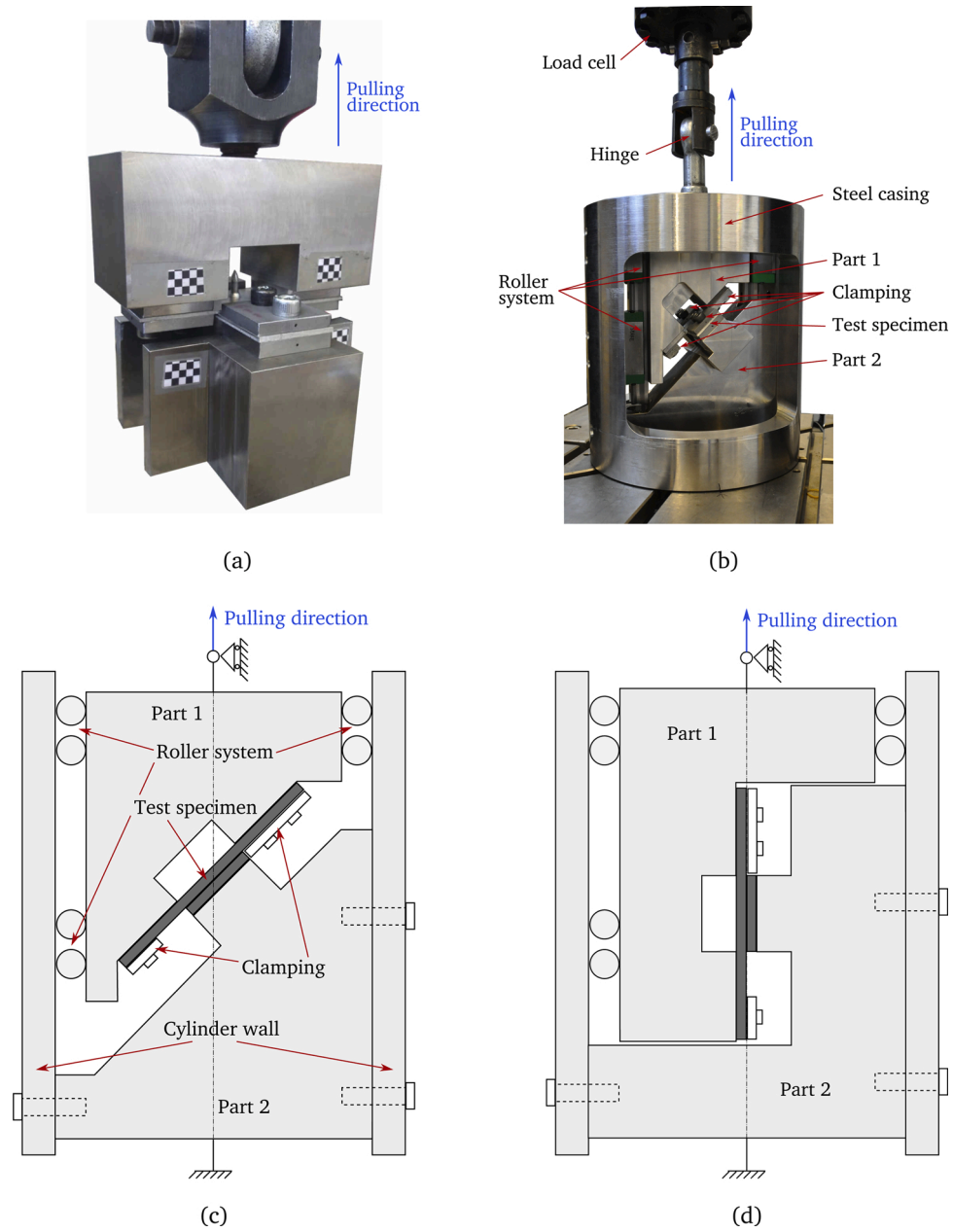

Fig. 8. Test configurations for the cross tensile tests (a) and for the loading at 45 degrees using a custom test rig (b). Schematic representations of the working principle of the cross rig for mixed mode (c) and pure shear loading (d). Adapted from Sønstabø et al. (2018a).

higher ductility than those without it, motivated by the capacity of the hole to accommodate the screw during its rotation. This difference in the confinement of the screw caused the maximum force to be lower in the pilot hole configuration, because the screw had more flexibility to rotate. In the tests without pilot hole, a higher stiffness caused higher forces that, in turn, led to screw failure (see Fig. 12e). In line with the results of the cross-shear tests, the head of the screw detached from the shank under a combination of shear and tensile forces. No screw failure was observed in any of the tests with a pilot hole, as shown in Fig. 12c.

4.3. Peeling tests

With the aim of evaluating the performance of the joints under tensile-dominated loads, peeling specimens were assembled and tested in the same machine and with the same configuration as the single-lap specimens. The dimensions of the peeling specimens are provided in Fig. 7c. Due to the deformation of the aluminium plates, the connection is subjected to a certain amount of shear force in addition to the tensile load.

As for the single-lap tests, four repetitions were run for the pilot hole and the no pilot hole configurations, being recorded by two cameras. The force-displacement curves are shown in Fig. 12b, where the initial length of the virtual DIC extensometer centred at the interface between the two plates was 80 mm.

With the exception of one single specimen showing an early failure, the differences in the mechanical behaviour of the joints with and without a pilot hole were less significant than those observed in the single-lap tests. In this tensile-dominated scenario, the maximum force was similar for both configurations, with the displacement at failure being slightly lower in the specimens without a pilot hole. It is also worth noticing the drop in the force at a displacement around 20 mm in these specimens, corresponding to the sliding between the screw and the top plate enabled by the pilot hole when the shear component of the load started to increase. The failure mode consisted of the screw thread being

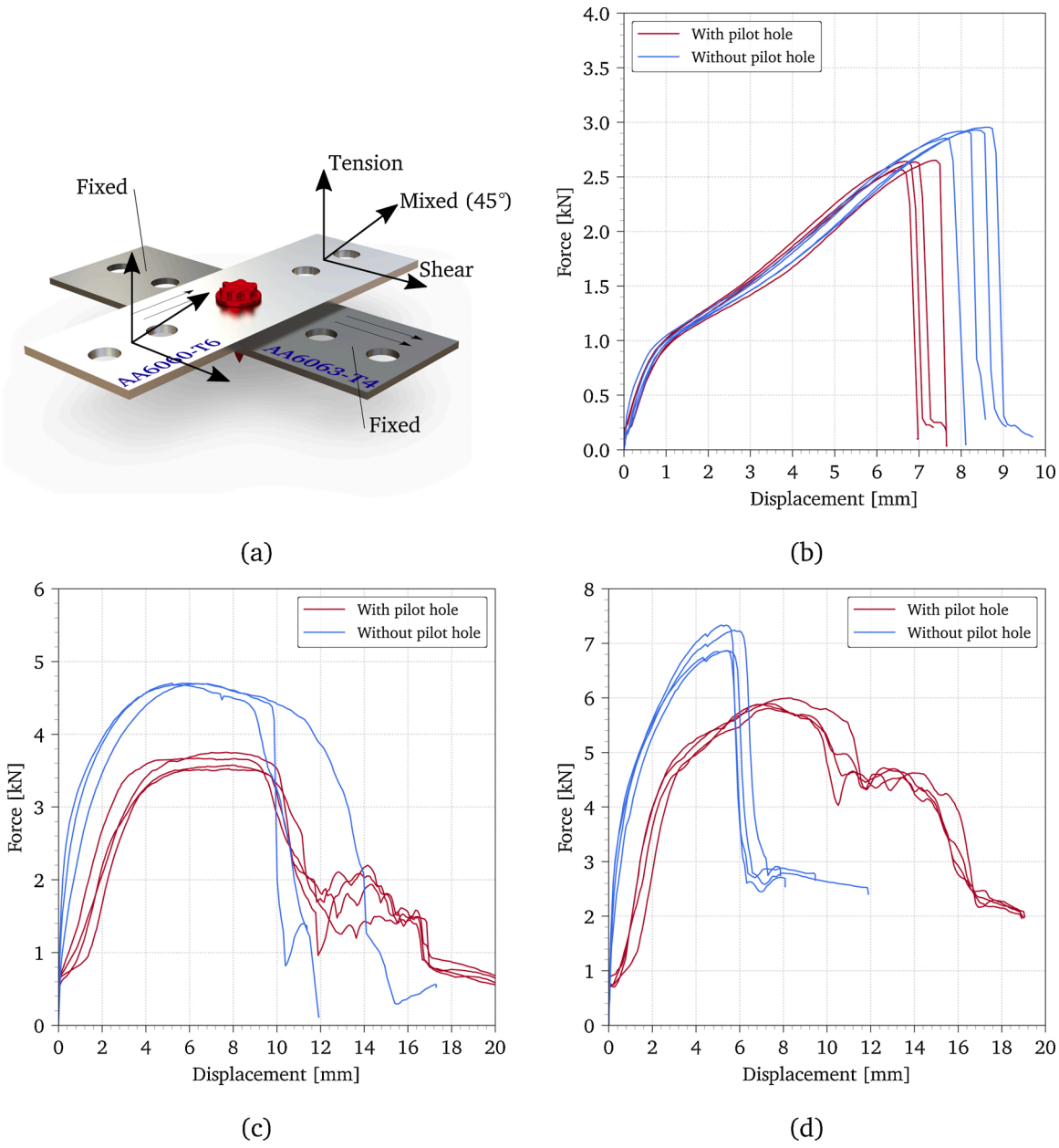

Fig. 9. Loading scheme of the cross tests (a) and force-displacement curves of the cross-tension (b), cross-mixed (c) and cross-shear tests (d) with and without pilot holes.

detached from the bottom plate in both configurations, as shown in Fig. 12d and f.

5. Mesoscopic modelling

5.1. Finite element model and analysis configuration

Joint testing requires a considerable amount of time to machine the plates, assemble the connections, prepare the test rig, mount and dismount the specimens, etc. Moreover, post-processing the experimental results is not straightforward in most cases. It is because of this that reliable finite element models are particularly profitable when it comes to predict the mechanical behaviour of a structural connection. The accuracy of these predictions will to a large extent depend on the refinement level of the finite element model, since a complex combination of contact, friction, plastic deformation and fracture takes place inside the joint.

A detailed finite element model of the cross tests was built in Abaqus/Explicit 2019, herein referred to as *mesoscopic model*. This model consisted of a solid-element model of one half of the test specimen, taking advantage of the symmetry of the problem. Two simplifications of the screw geometry were made in order to have a topology with circular symmetry: the helix was neglected and the complex surfaces of the head were simplified. Sønstabø et al. (2018a) showed that the first simplification still gives reasonable results, and the simplification of the head was done in a way such that the moment of inertia of the simplified geometry with respect to the axis of the screw was equal to that of the original head. A complete view of the mesoscopic model is shown in Fig. 13a, where the clamps have been omitted for clarity. The models have around 225,000 linear, 8-node solid elements with reduced integration, the smallest element size being around 100 μm. Adequate hourglass control was enforced to prevent spurious deformation modes owing to the reduced integration scheme. Special care was taken regarding the mesh of the screw, where the 8-node element mesh was

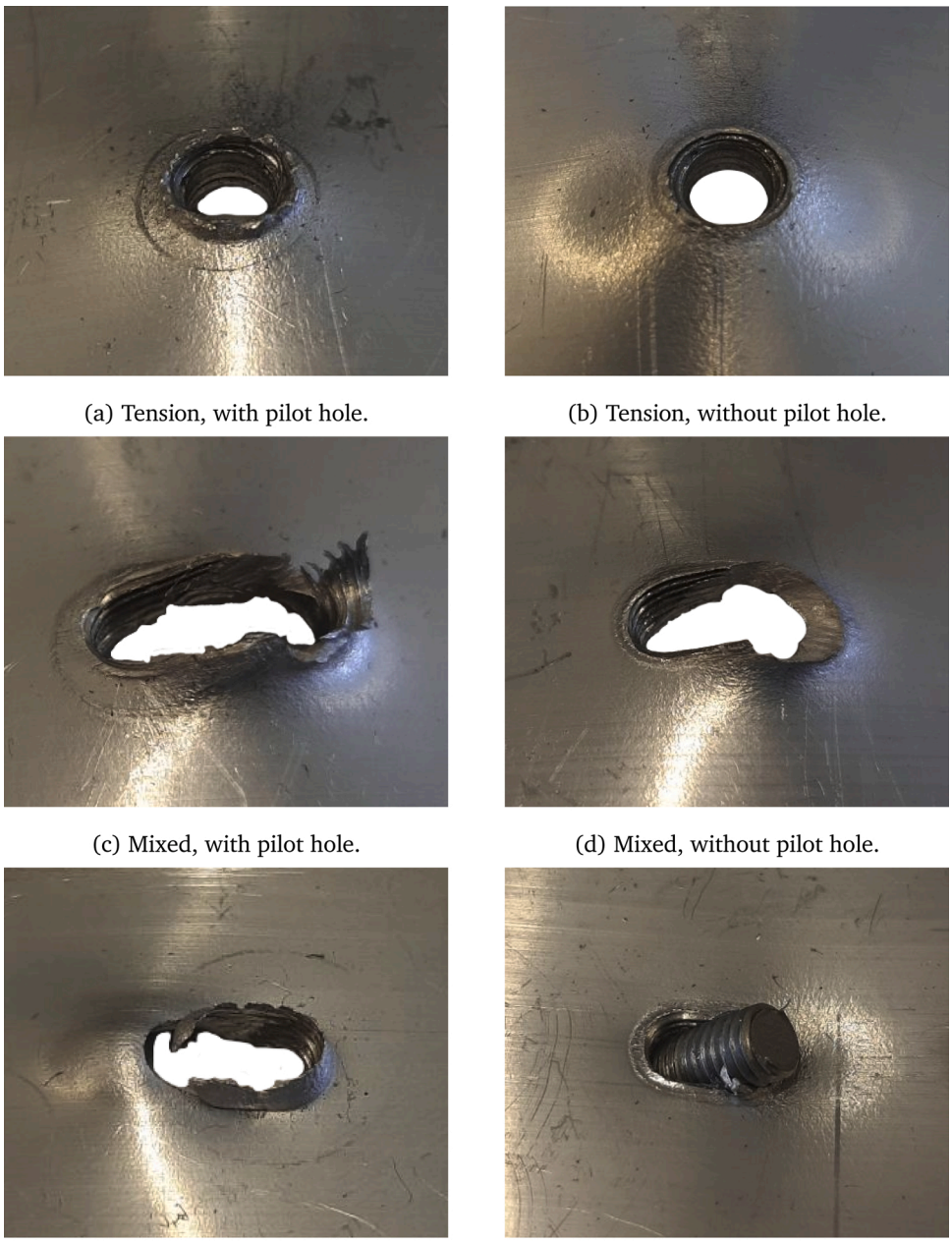

(a) Tension, with pilot hole. (b) Tension, without pilot hole.

(c) Mixed, with pilot hole. (d) Mixed, without pilot hole.

(e) Shear, with pilot hole. (f) Shear, without pilot hole.

Fig. 10. Details of the post-mortem cross specimens, bottom plate.

created with an ad hoc Python script to have the same element size as that used in the material calibration. It can be observed how the mesh inside the screw was refined in the region where failure took place. Fig. 13.

The clamps were modelled as rigid parts in contact with the specimen, as shown in Fig. 13b. The friction coefficient was set to 0.2 in the whole model through a general contact algorithm, with the exception of the contact between clamps and specimen, where this value was increased to 0.6 to reduce the relative displacements between both parts. It is worth mentioning that one of the two clamps had to be modified in the simulations of cross-shear and mixed modes to account for the shorter clamp used in these tests, where enough room had to be left for the moving part to travel without colliding the clamping system.

The case-hardened layer on the surface of the screws was also included in the model, as shown in Fig. 13c and d, with the same dimensions as those used in the calibration of the outer W_c.

Due to the complexity of the problem and the level of refinement of the mesh, the simulations were sped up by means of a combination of time- and mass-scaling. A time scaling factor of 100 was applied in all simulations, meaning that the simulated time was 100 times shorter than the time required for one experimental test. Additionally, selective mass-scaling was applied to those elements undergoing severe deformations so that they do not harm the computational performance of the model. Elements requiring stable time increments below 5 μs got their densities artificially increased to keep the overall stable increment around or above the target value. With this configuration, the analyses took around 5–7 h to run on a high-end, multi-core workstation. These CPU times could be reduced to some extent with a coarser mesh in the clamped areas, but an optimisation of the computational performance was not carried out in the present study. Despite the time and mass scaling, quasi-static conditions were ensured by smoothly applying the displacement to the moving clamp and by a kinetic energy check.

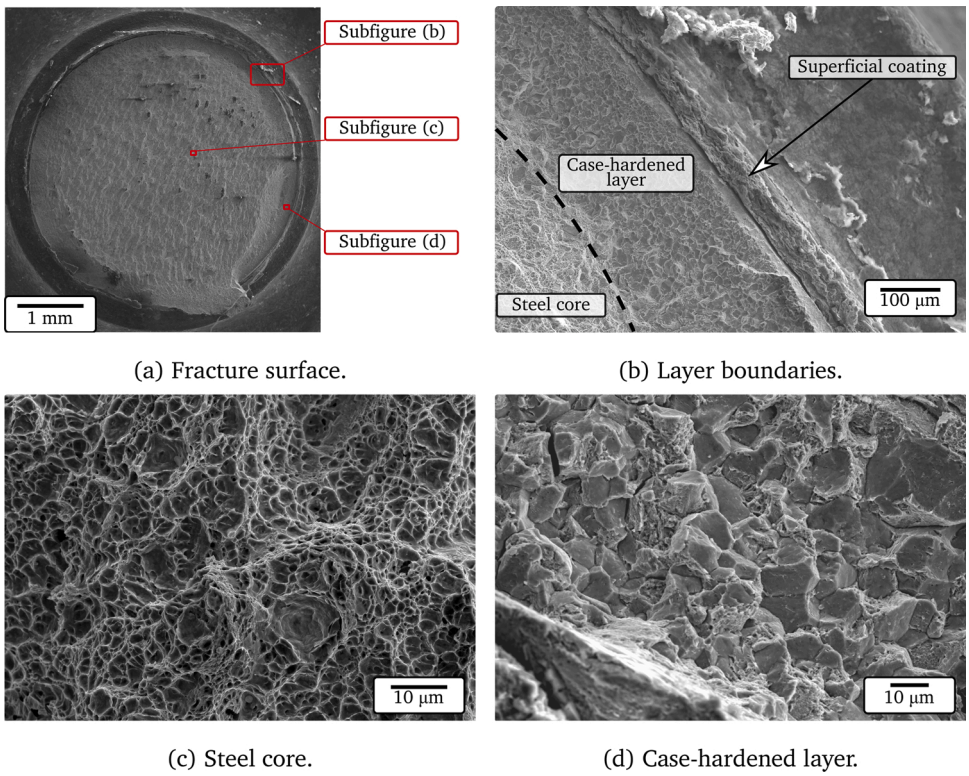

(a) Fracture surface. (b) Layer boundaries.

(c) Steel core. (d) Case-hardened layer.

Fig. 11. Scanning electron microscopy images of the fracture surface of the screw in the cross-shear tests without pilot hole.

5.2. Determination of the modelled extrusion length

The geometry of the interface between the screw and the plates is one of the key aspects of this kind of mesoscopic model. The finite element model required careful definition in this area based on cutaway pictures of the connection with and without a pilot hole, see Fig. 3a and b. It is important to highlight that the threads in the real connection were not fully engaged, especially in the connection with a pilot hole, and that the aluminium was markedly altered at the end of the extrusions. Owing to these reasons, the mesoscopic models used in this investigation had a reduced extrusion length compared to what was observed in the cutaway pictures, as it can be observed in Fig. 13c and d. This reduction is particularly noticeable in the connection with the pilot hole, since part of the aluminium drilled out from the bottom plate was accommodated in the gap of the pilot-hole without having a mechanical contribution. In the configuration without pilot hole, this material encounters the constraint of the top plate and is ejected downwards to a larger extent.

Both the material degradation and the partial engagement are a function of the process parameters when screws are applied (speed, torque, etc.), and also of the original material properties and thickness of the plates. Therefore, the effective extrusion length to be accounted for in the finite element models had to be estimated for this particular case. This determination was done by trial and error, and a remarkable sensitivity was observed. The models were run in three configurations. In the first case, the length of the lower extrusion was the apparent length measured from the cutaway pictures of the joint. In the second case, the length was reduced and it was comparable to the fraction of the thread with effective engagement in the cutaway pictures. In the third case, both the boss and the extrusion were totally removed from the model. These modifications are illustrated in Fig. 14a and b for the configurations with and without pilot holes. Simulations of the cross-tests with and without pilot hole were run under tension and shear, yielding the force-displacement curves shown in Fig. 14. The experimental curves are included in the plots.

It can be observed how sensitive the model was to a change in the length of the extruded material, with peak forces ranging between 90 and 125 % and displacements at failure ranging between 70 and 160 % of the reference experimental values, approximately. In the cross-tension tests, the model with the apparent extrusion length provided additional grip after the plates started to bend and the top part of the thread started to open, increasing the force and displacement at failure and also the stiffness along the test, as shown in Fig. 14c and d. The opposite effect was achieved by removing the extrusion and boss from the model. In the cross-shear case, the extrusion length mainly affected the point at which the screw shank failed. Longer extrusions provided more bending moment on the screw as the resultant forces of each plate were moved away from each other, thus causing an earlier failure. Removing the extrusion had the opposite effect, delaying screw failure (Fig. 14f). In view of these results, it was deemed reasonable to reduce the modelled extrusion length to an effective length which accounted only for the fully engaged thread observed in the cutaway pictures, Fig. 13c and d.

5.3. Summary of assumptions

Before presenting the results of the mesoscopic models, a list of all the assumptions made during the modelling process is provided next.

- The mechanical properties of the aluminium plates were considered homogeneous, despite the variations in hardness shown in Fig. 3. The thermomechanical and microstructural histories of the flow-drilling process were not accounted for.
- The case-hardening of the screws was modelled with two material models –one for the outer surface of the screw, and another one for the inner part–, rather than using a smooth gradient from the surface to the inside. The mechanical properties in each of these two regions were assumed homogeneous.
- Isotropic mechanical properties were assumed in all materials.
- The geometry of the screw was simplified adopting a simpler head with an average moment of inertia, and neglecting the helix angle.

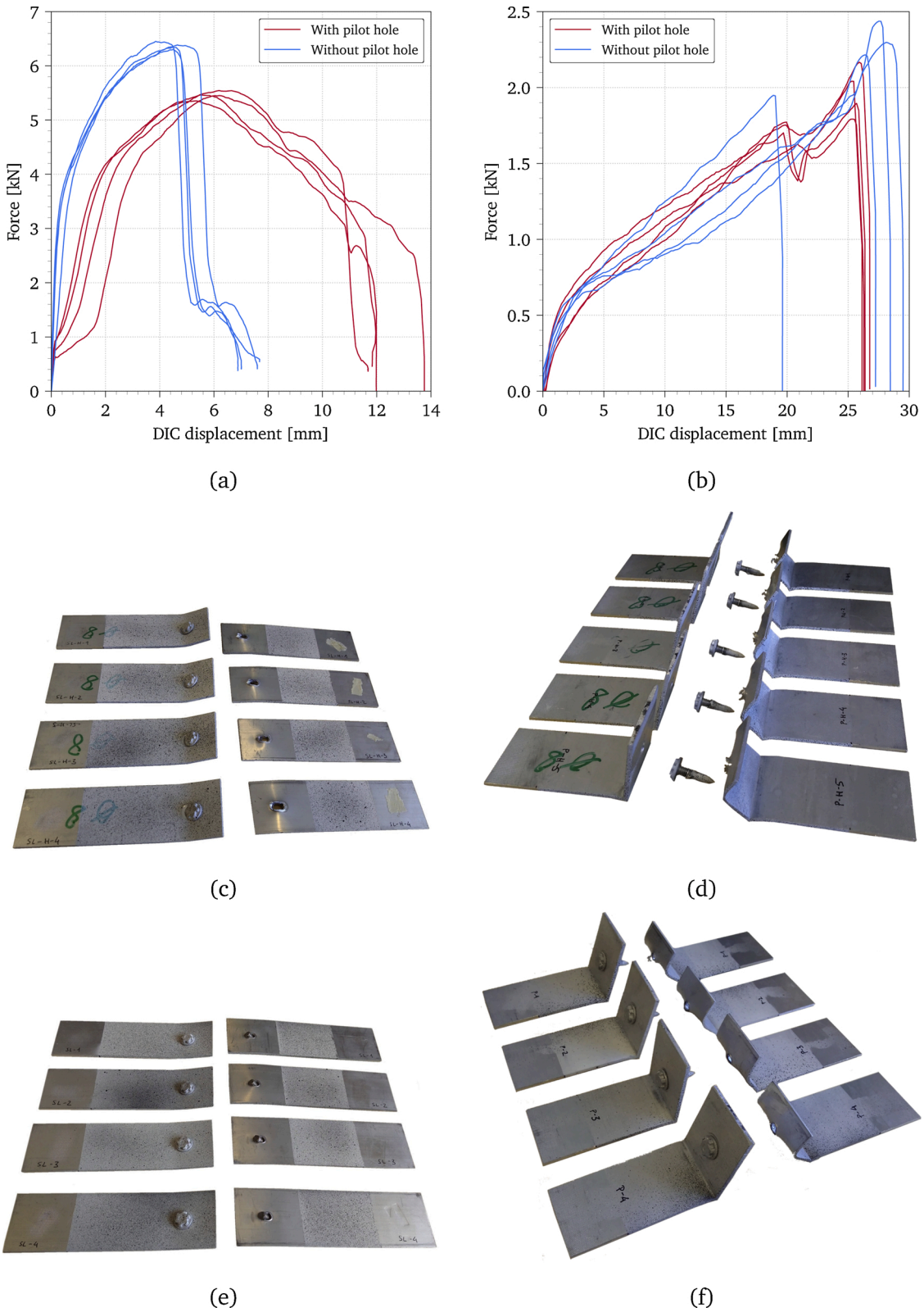

Fig. 12. Force-displacement curves of the single-lap (a) and peeling tests (b). Post-mortem single-lap specimens with pilot hole (c), without pilot hole (e), peeling with pilot hole (d) and without pilot hole (f).

- The length of the extrusions generated during the assembly of the screw was reduced compared to that in the cutaway pictures of the samples in order to exclude material with marginal mechanical contribution.

5.4. Mesoscopic model results

Comparison of the force-displacement curves obtained with the mesoscopic models and the corresponding cross tests is provided in Fig. 15, where the force and displacement axes have equal sizes for an

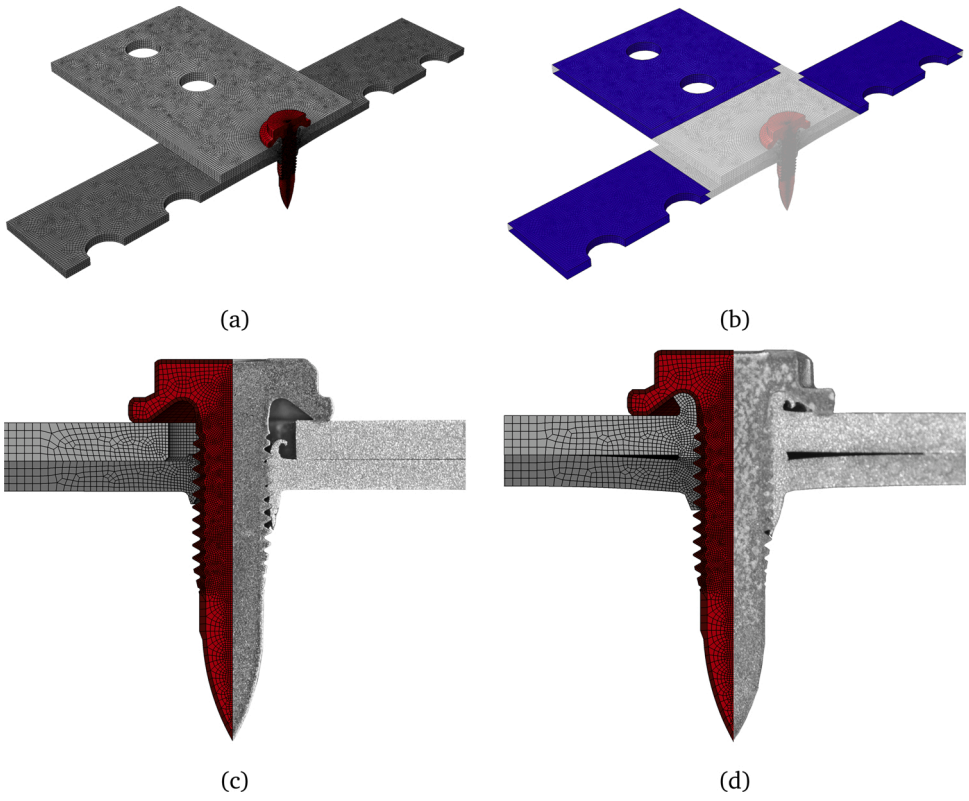

Fig. 13. Images of the mesoscopic finite element model: general view (a), rigid clamping parts for the cross-tension simulation (b), and detail of the mesh at the connection for the configurations with (c) and without pilot hole (d) compared to the real geometry of the samples.

easier comparison. The models incorporated the effective length determined in the previous section. Excellent agreement between numerical simulations and experiments was achieved in all cases. Screw failure was quite accurately predicted in the simulation of the cross-shear tests without pilot hole, Fig. 15b, but the models also predicted fracture in the screw at the very end of the cross-shear tests with pilot hole. Post-mortem analyses of the corresponding specimens revealed severe bending deformation of the screw in the latter, so it is reasonable to think that the steel almost reached failure in the experiments. Thus, the predictions of the mesoscopic model were slightly conservative in this vein.

It is also interesting to comment on the different start of the curves in Fig. 15a corresponding to the shear loading mode with pilot hole. In this simulation, the position of the top plate was adjusted so that it started in contact with the screw, saving some simulation time. On the contrary, the force rapidly increased to 0.9 kN at the beginning of the experiments due to the pre-tensioning of the screw, which was not accounted for in the simulations. A similar phenomenon could be observed to a lesser degree in the mixed mode loading, where the pre-tensioning of the joint made the initial response stiffer in the tests than in the simulation.

The results of the mesoscopic models provided additional insight about the deformation and failure mechanisms of the connection. The cross-tensile simulations showed the same behaviour as the experimental tests, with the bottom plate bending and the screw becoming gradually detached from the threaded aluminium as the separation between the two plates increased. Fig. 16a and 16 b show the models with and without pilot hole at failure, respectively. The colour maps represent the computed equivalent plastic strain. The extra length of the lower extrusion in the joint without pilot hole is what made that failure took place a bit later than in the pilot hole configuration.

Also in line with the experiments, the cross-shear mesoscopic models differed when comparing the configurations with and without pilot hole. In the first case, Fig. 16c, the screw rotated inside the connection. This rotation was enabled by the pilot hole, which provided enough room to accommodate part of the screw head during rotation. The failure mode consisted of a through-thickness shear failure of the bottom plate, even though the screw failed at the end of the simulations, when it slid over the bottom plate. This discrepancy in the tests where no screw failure was observed was most likely due to the characteristics of the Cockcroft-Latham failure criterion used for the aluminium plates. From its definition, Eq. (7), it can be seen that the damage variable only increases if the first principal stress is positive. Fig. 16c shows that the right part of the bottom plate was clearly compressed, with equivalent plastic strains around 2. However, damage did not start to accumulate in these elements until the screw started to slide, due to the nature of the failure criterion. It is believed that a failure criterion computing damage under compression-dominated loading would have damaged the material in this area, enabling the sliding of the screw without any failure in the steel.

The failure of the connection without pilot hole under pure shear is illustrated in Fig. 16d, which clearly depicts how the shank of the screw fractures under bending combined with shear. This extra bending compared to the pilot hole configuration stems from the absence of a hole where the head of the screw could be accommodated during its rotation, and starts when the brittle case-hardened layer cracks. Additional simulations run with the outer layer incorporating the same material model as the core of the screw showed that the strength of this particular connection could be largely increased, since the screw did not fail in this case. However, case-hardening of the screw seems to be customary to guarantee that it perforates the plates during assembly. Whether other alternative treatments would increase the resistance of its outer layer without decreasing its ductility is left as an open question.

The local deformation mechanisms observed in the experimental tests were also well captured by the mesoscopic models. As an example, Fig. 17 compares the characteristic tearing of the bottom plate in simulations and tests (Fig. 17a and b), and the local deformation of the top

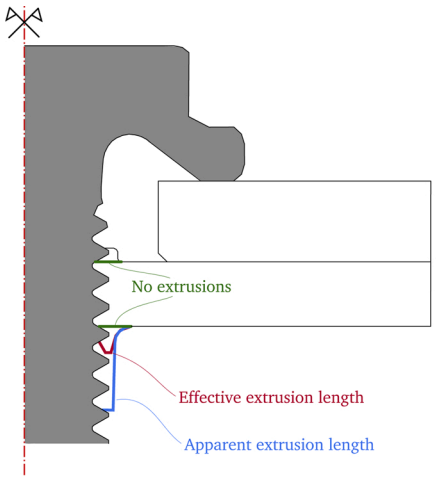

(a) Modifications with pilot hole.

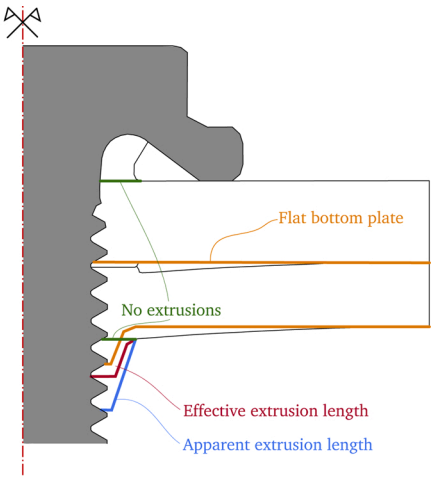

(b) Modifications without pilot hole.

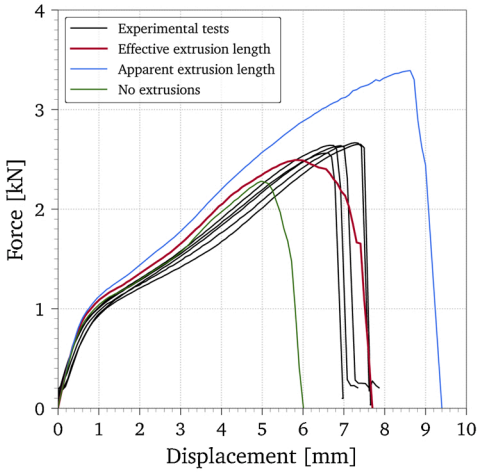

(c) Tension with pilot hole.

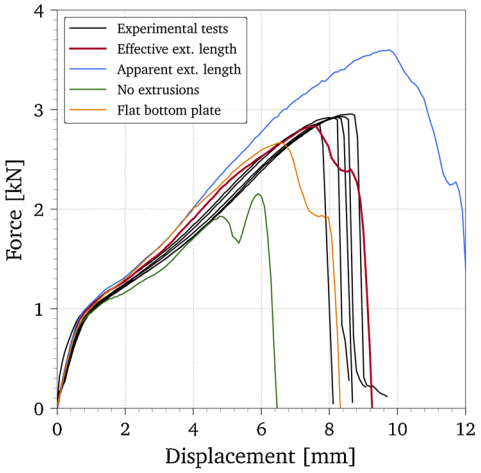

(d) Tension without pilot hole.

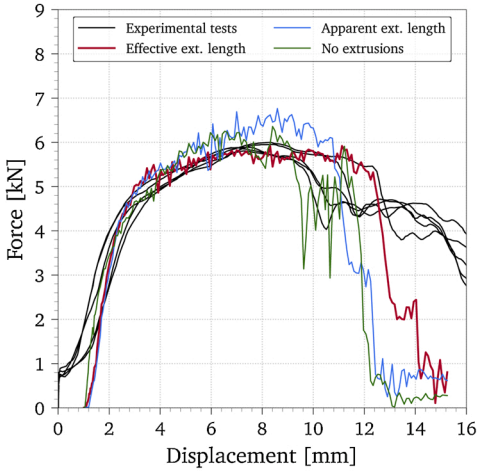

(e) Shear with pilot hole.

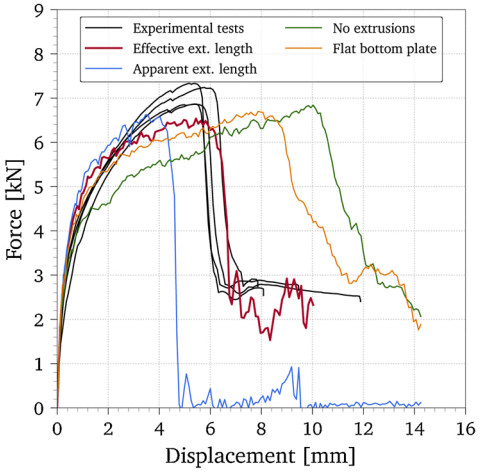

(f) Shear without pilot hole.

Fig. 14. Sensitivity of the mesoscopic models to geometrical variations in the extrusion lengths and the curvature of the bottom plate.

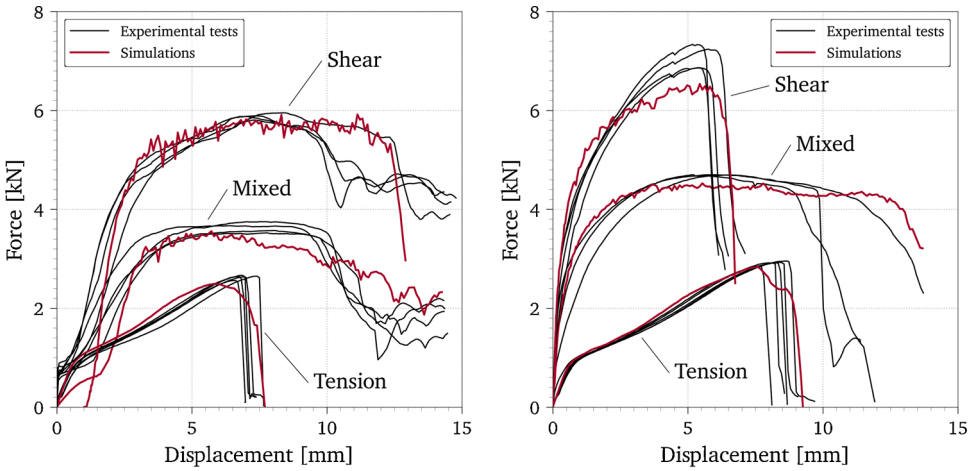

(a) With pilot hole. (b) Without pilot hole.

Fig. 15. Force-displacement curves obtained with the mesoscopic models and the experimental cross tests.

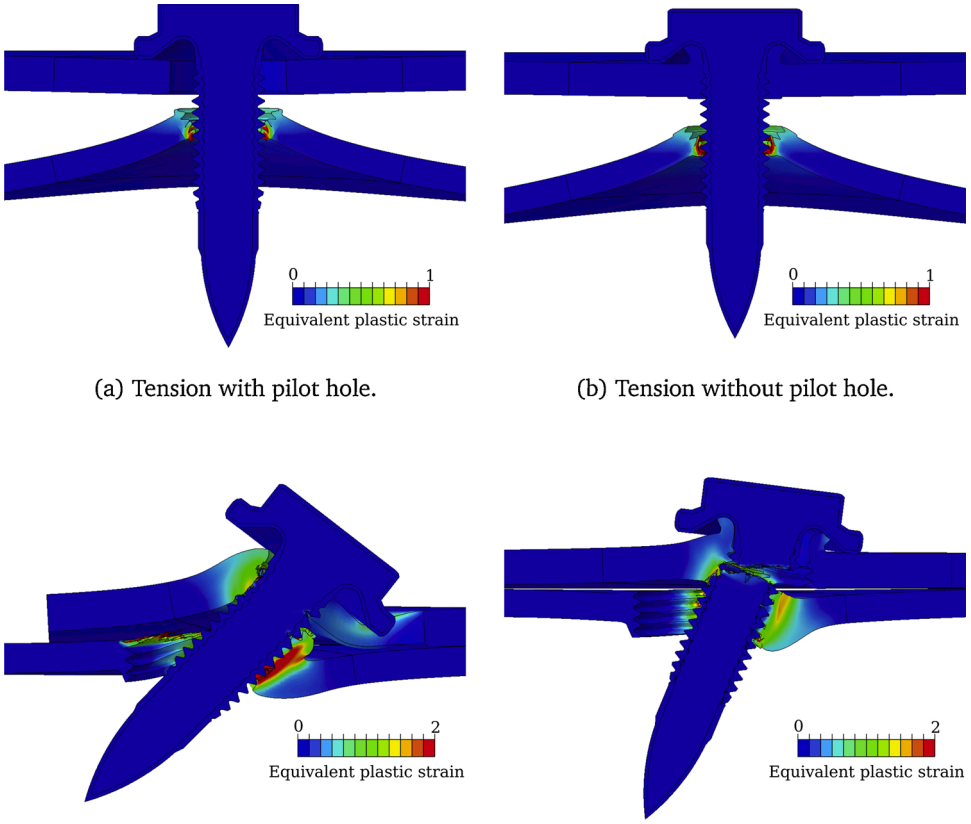

(a) Tension with pilot hole. (b) Tension without pilot hole.

(c) Shear with pilot hole. (d) Shear without pilot hole.

Fig. 16. Contours of equivalent plastic strain on the deformed finite element model at failure. The mesh has been removed for a clearer display. (For interpretation of the references to color in the text, the reader is referred to the web version of this article.)

plate in the shear tests, Fig. 17c and d. Therefore, the model gave good predictions of the experiments both quantitative and qualitatively.

5.5. Discussion and robustness of the mesoscopic results

Comparison of numerical predictions and experimental tests showed that the mesoscopic model can provide accurate results, and that the mechanics of the joints were well captured. However, many different models had to be built before finding the final configuration. While being time-consuming, these iterations allowed to assess the importance of accounting for or neglecting some features of the connection when said models are to be built. In addition to the determination of an effective extrusion length presented in Section 5.2, the influence of other geometrical features was investigated and reported in the current section.

A gap between the connected plates can be generated during the

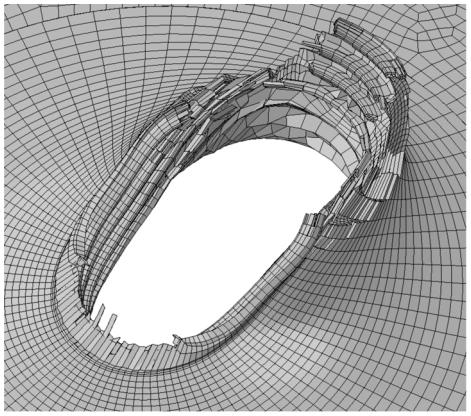

(a) Mixed mode with pilot hole, bottom plate.

(b) Mixed mode with pilot hole, bottom plate.

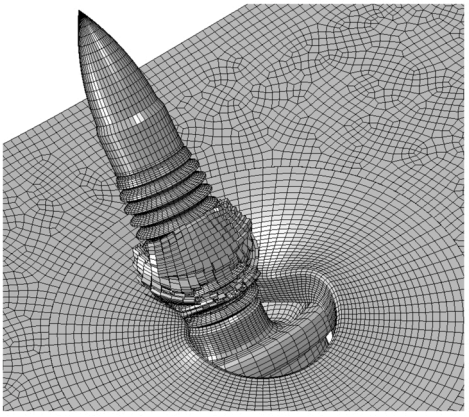

(c) Shear with pilot hole, screw and top plate.

(d) Shear with pilot hole, screw and top plate.

Fig. 17. Details of the deformed finite element model (left) and the experimental specimens (right). Bottom plate tearing and through-thickness shear failure in the mixed mode with pilot hole, (a) and (b); and tearing and partial penetration of the screw head into the pilot hole under shear, (c) and (d).

assembly of FDS joints without pilot hole, due to the partial extrusion of material at the interface and the final tightening of the screw, Fig. 3b. Usually, the plate with a lower bending stiffness becomes bent (in this case the bottom plate). The resulting curvature of the bottom plate was included in in the mesoscopic model, but since this is also difficult to measure or predict without cutting a sample, it seemed worth studying if the models could give reasonable predictions with a totally flat bottom plate. The mesoscopic model without pilot hole was run again to verify this point with a flat bottom plate and the original extrusions, as illustrated in Fig. 14b, and the results were added to the force-displacement plots in Fig. 14d and f. It can be seen that flattening the bottom plate had a similar effect to that obtained by reducing the extrusion length. In particular, the peak tensile forces were lowered due to a less stiff geometry of the bottom plate, and screw failure was delayed. For the studied connection, it has been shown that this curvature matters and should be included in the mesoscopic model.

As it was mentioned, the gap between both plates hosts a fraction of material expelled during the penetration of the screw and the formation of the thread, as shown in Fig. 3b. This material was included in the model, with the boundary between both plates at its middle line. Given the cutaway view, it could seem reasonable to tie this boundary and unite both plates. However, experimental observations suggested otherwise. This point was verified by running simulations with both surfaces tied or free to move independently. Even though the curves are not plotted here for the sake of brevity, it could be seen that tying both plates together at this point overpredicted the resultant forces by approximately 30 %. It is therefore advisable to enable relative displacement between the plates at this location. Two additional simulations were run shifting the interface between the plates up or down, i.e., making the material in the gap belong to either the top or the bottom plate completely. This produced only marginal differences in the results, only affecting slightly the behaviour under tension due to a shorter or longer threaded length in the bottom plate.

The final geometrical feature checked with additional simulations was the boss extruded upstream and hosted under the screw head in the no-prehole configuration. It was found that its mechanical contribution is quite relevant as it acts as an additional constraint on the screw, reducing its rotation (observe how some plastic straining appears in these areas during shearing, Fig. 16d). Including this fraction of material was important to predict the correct failure point in the screw in the cross-shear simulations.

6. Conclusions

A thorough study on the mechanical performance of flow-drill screw joints with and without pilot holes was conducted. The studied joints were made of two aluminium plates joined together with a flow-drill screw made of case-hardened, high-strength steel. The top plate was

made of an AA6060-T6 aluminium alloy with a nominal thickness of 2.5 mm, whereas the bottom plate was made of AA6063-T4 with a nominal thickness of 2.0 mm. The investigation included material tests, joint tests in several configurations and numerical modelling at a mesoscopic scale. The following conclusions can be drawn:

- It has been shown how incorporating a pilot hole increases the ductility and decreases the maximum force of the connection under shear-dominated loading, while the mechanical response under pure tension is only marginally altered.
- Screw failure has been reported in shear-dominated loading of the connections without pilot hole. It has been shown how the additional confinement of the screw in this configuration leads to higher bending loads that can lead to early failure of the screw.
- Case-hardening of the outer layer of the screw seems to promote screw failure under shear loading modes. This layer is harder but also more brittle. Under high bending loads, tensile stress on the surface produced a crack that rapidly propagated across the whole cross-section of the screw, producing the aforementioned early failure.
- The relevance of several geometrical features for a correct modelling at mesoscopic scale has been assessed. In particular, determining an effective extrusion length has been proven crucial for an accurate prediction of the experimental behaviour.

The previous conclusions are obtained through the results of a detailed mesoscopic model of the connection with and without pilot holes. It has been shown how these kind of detailed models provide meaningful information about the deformation mechanics and kinematics of the connection, and are able to estimate the global force-displacement response with a good degree of accuracy. This could potentially decrease the number of experimental tests required to characterise flow-drill screw joints in an industrial context.

CRediT author statement

Miguel Costas: conceptualization, methodology, software, validation, formal analysis, investigation, writing, visualization.

David Morin: conceptualization, software, resources, supervision, project administration, funding acquisition.

Johan Kolstø Sønstabø: methodology, supervision.

Magnus Langseth: resources, supervision, project administration, funding acquisition.

Declaration of interests

None declared.

Declaration of Competing Interest

The authors report no declarations of interest.

Acknowledgements

The authors would like to acknowledge the financial support from the Centre for Advanced Structural Analysis (CASA) (Project No. 237885) funded by the Research Council of Norway and NTNU. Fruitful discussions with Jakub Gałązka and Satoru Miyagano from Toyota Motor Europe and with the staff at Ejot helped to develop this work. The microscope images of the samples, together with the hardness tests and the microstructure analyses were performed at Centro Nacional de Investigaciones Metalúrgicas (CENIM) of Consejo Superior de Investigaciones Científicas (CSIC) in Madrid (Spain) by Dr. María Jesús Bartolomé, to whom the authors are grateful. Credit for the priceless assistance at the lab must be given to Mr. Tore Wisth and Mr. Trond Auestad. Thanks to Ms. Maisie Edwards-Mowforth for correcting grammatical errors and spelling mistakes.

References

Aslan, F., Langlois, L., Balan, T., 2019. Experimental analysis of the flow drill screw driving process. Int. J. Adv. Manuf. Technol. 104, 2377–2388.
Barlat, F., Aretz, H., Yoon, J.W., Karabin, M.E., Brem, J.C., Dick, R.E., 2005. Linear transfomation-based anisotropic yield functions. Int. J. Plast. 21 (5), 1009–1039.
Bouchard, P.O., Laurent, T., Tollier, L., 2008. Numerical modeling of self-pierce riveting-From riveting process modeling down to structural analysis. J. Mater. Process. Technol. 202 (1), 290–300.
Chen, N., Luo, H., Wan, M., Chenot, J.-L., 2014. Experimental and numerical studies on failure modes of riveted joints under tensile load. J. Mater. Process. Technol. 214 (10), 2049–2058.
Cockcroft, M.G., Latham, D.J., 1968. Ductility and the workability of metals. J. Inst. Metals 96, 33–39.
Costas, M., Morin, D., Hopperstad, O.S., Børvik, T., Langseth, M., 2019. A through-thickness damage regularisation scheme for shell elements subjected to severe bending and membrane deformations. J. Mech. Phys. Solids 123, 190–206.
Engler, O., Marioara, C.D., Aruga, Y., Kozuka, M., Myhr, O.R., 2019. Effect of natural ageing or pre-ageing on the evolution of precipitate structure and strength during age hardening of Al-Mg-Si alloy AA 6016. Mater. Sci. Eng.: A 759, 520–529.
Fagerholt, E., Børvik, T., Hopperstad, O.S., 2013. Measuring discontinuous displacement fields in cracked specimens using digital image correlation with mesh adaptation and crack-path optimization. Optics Lasers Eng. 51 (3), 299–310.
Holmen, J.K., Solberg, J.K., Hopperstad, O.S., Børvik, T., 2017. Ballistic impact of layered and case-hardened steel plates. Int. J. Impact Eng. 110, 4–14.
Khadyko, M., Myhr, O.R., Hopperstad, O.S., 2019. Work hardening and plastic anisotropy of naturally and artificially aged aluminium alloy AA6063. Mech. Mater. 136, 103069.
Kim, J., Lee, H., Choi, H., Lee, B., Kim, D., 2020. Prediction of load-displacement curves of flow drill screw and RIVTAC joints between dissimilar materials using artificial neural networks. J. Manuf. Process. 57, 400–408.
Kong, X., Yang, Q., Li, B., Rothwell, G., English, R., Ren, X.J., 2008. Numerical study of strengths of spot-welded joints of steel. Mater. Des. 29 (8), 1554–1561.
Liu, W., Zhu, X., Zhou, Q., He, H., Liu, J., Xu, C., Li, L., 2020. Modeling and simulation of the flow drill screw process of a DP590/Al6061-T6 multi-material joint used for vehicle body. Int. J. Adv. Manuf. Technol. 110, 1189–1201.
Livermore, 2015. Software Technology Corporation. LS-OPT User's Manual, version 5.2. Livermore, California.
Myhr, O.R., Grong, Ø., Schäfer, C., 2015. An extended age-hardening model for Al-Mg-Si alloys incorporating the room-temperature storage and cold deformation process stages. Metall. Mater. Trans. A 46, 6018–6039.
Nielsen, K.L., 2008. 3D modelling of plug failure in resistance spot welded shear-lab specimens (DP600-steel). Int. J. Fract. 153, 125–139.
Nielsen, K.L., Tvergaard, V., 2010. Ductile shear failure or plug failure of spot welds modelled by modified Gurson model. Eng. Fract. Mech. 77 (7), 1031–1047.
Pandya, K.S., Grolleau, V., Roth, C.C., Mohr, D., 2020. Fracture response of resistance spot welded dual phase steel sheets: experiments and modeling. Int. J. Mech. Sci. 187, 105869.
Simulia, 2018. ABAQUS 2019 Documentation. Providence Road, Rhode Island.
Skovron, J., Mears, L., Ulutan, D., Detwiler, D., Paolini, D., Baeumler, B., Claus, L., 2014. Characterization of flow drill screwdriving process parameters on joint quality. SAE Int. J. Mater. Manf. 8 (09), 35–44.
Skovron, J.D., Prasad, R.R., Ulutan, D., Mears, L., Detwiler, D., Paolini, D., Baeumler, B., Claus, L., 2015. Effect of thermal assistance on the joint quality of Al6063-T5A during flow drill screwdriving. J. Manuf. Sci. Eng. 137 (5), 051019.
Sønstabø, J.K., Holmstrøm, P.H., Morin, D., Langseth, M., 2015. Macroscopic strength and failure properties of flow-drill screw connections. J. Mater. Process. Technol. 222, 1–12.
Sønstabø, J.K., Morin, D., Langseth, M., 2016. Macroscopic modelling of flow-drill screw connections in thin-walled aluminium structures. Thin-Walled Struct. 105, 185–206.
Sønstabø, J.K., Morin, D., Langseth, M., 2018a. Testing and modelling of flow-drill screw connections under quasi-static loadings. J. Mater. Process. Technol. 255, 724–738.
Sønstabø, J.K., Morin, D., Langseth, M., 2018b. Static and dynamic testing and modelling of aluminium joints with flow-drill screw connections. Int. J. Impact Eng. 115, 58–75.
Szlosarek, R., Karall, T., Enzinger, N., Hahne, C., Meyer, N., 2013. Mechanical testing of flow drill screw joints between fibre-reinforced plastics and metals. Mater. Test. 55 (10), 737–742.